RSC Advances

PAPER

View Article Online
View Journal | View Issue

Cite this: *RSC Adv.*, 2022, **12**, 5164

A novel electrochemical sensor for glyphosate detection based on $Ti_3C_2T_x$/Cu-BTC nanocomposite

Shan Wang,[a] Yanqing Yao,[a] Jia Zhao,[a] Xuhui Han,[a] Chunpeng Chai *[a] and Pei Dai*[b]

Received 3rd November 2021
Accepted 1st February 2022

DOI: 10.1039/d1ra08064d

rsc.li/rsc-advances

The copper benzene-1,3,5-tricarboxylate (Cu-BTC) with outstanding chemical and physical properties, is a novel and promising material in the field of electrochemical sensing. However, it has significant limitations for direct application in electrochemical sensing due to the relatively weak conductivity of Cu-BTC. Here, the conductivity of Cu-BTC was improved by loading Cu-BTC onto two-dimensional $Ti_3C_2T_x$ nanosheets with high conductivity. Thanks to the synergistic effect produced by the high conductivity of $Ti_3C_2T_x$ and the unique catalytic activity of Cu-BTC, the $Ti_3C_2T_x$/Cu-BTC nanocomposite exhibits excellent sensing performance for glyphosate, with a low limit of detection (LOD) of 2.6×10^{-14} M and wider linear sensing range of 1.0×10^{-13} to 1.0×10^{-6} M. Moreover, the electrochemical sensor based on $Ti_3C_2T_x$/Cu-BTC also shows excellent selectivity, good reproducibility and stability.

1. Introduction

Glyphosate (*N*-(phosphonomethyl)glycine) is a broad-spectrum, non-selective organophosphorus herbicide, which is widely used in the field of weed and vegetation control in agriculture, industry and household use.[1–5] With the advancement of productivity, industry and agriculture have generally achieved automation, the use of glyphosate and other pesticides has also increased day by day, and the potential harm of glyphosate has also attracted more and more attention.[6,7] Although there are still controversies about whether glyphosate is carcinogenic, the long-term and large-scale use of glyphosate has caused harm to humans, animals, plants, and the environment. Therefore, it is necessary to develop a simple, efficient, and highly selective method for detecting glyphosate.

Compared with liquid chromatography, gas chromatography and other analytical sensing methods for glyphosate, electrochemical sensing has the advantages of low cost, simple operation, easy to carry, high sensitivity, and less sample consumption.[8–10] Although glyphosate is a non-electroactive compound and cannot be measured at an accessible potential, there have been reports of electrochemical sensing of glyphosate by modifying the electrode and processing the sample.[11–13] Prasad *et al.*[14] constructed an electrochemical sensor based on a graphite electrode modified by a dual-template imprinted polymer nanomembrane and used it to detect glyphosate in soil. The linear response range and the limit of detection of the sensor to glyphosate are 3.98–176.23 ng ml^{-1} and 0.35 ng ml^{-1}, respectively. Khenifi *et al.*[15] developed an electrochemical sensing platform based on NiAl-LDH layered double hydroxide (LDH) by co-depositing NiAl-LDH on the surface of the Pt electrode and applied it to glyphosate sensing. The detection mechanism is the electrocatalytic oxidation of Ni^{3+} in NiAl-LDH to the amine group in glyphosate. The LOD and linear response ranges of the sensor to glyphosate are 1×10^{-6} M and 1×10^{-5} to 9×10^{-4} M, respectively. Although these methods provide new ideas for the electrochemical detection of glyphosate, there are still some problems such as complex preparation processes, high limit of detection, wide detection range and poor anti-interference and stability. Therefore, it is of great value to develop an electrochemical sensor for glyphosate detection with excellent comprehensive performance such as simple process, high detection efficiency, excellent anti-interference.

Metal–organic frameworks (MOFs) materials have a wide range of applications. Due to their large specific surface area, high porosity, controllable structure and abundant active metal sites,[16–18] MOFs materials are widely used in the fields of adsorption–separation, gas storage and catalysis.[19–21] And it is worth noting that in recent years, MOFs have been used more as electrochemical sensing platforms to detect certain substances, such as hydrogen peroxide,[22,23] dopamine,[24,25] hydrazine[26,27] and ascorbic acid.[28,29] Cu-BTC is a kind of MOFs material formed by self-assembly of metal Cu^{2+} and organic ligand trimesic acid.[30–32] Ji *et al.*[33] first applied it to the electrochemical sensing of sunset yellow and lemon yellow. Cao *et al.*[34] creatively applied Cu-BTC to the electrochemical sensing of glyphosate. The sensing mechanism is based on the fact that the phosphate groups, amine groups and carboxyl groups in glyphosate easily

---

[a] *School of Materials Science and Engineering, Beijing Institute of Technology, Beijing 100081, China. E-mail: chaicp@bit.edu.cn*

[b] *Beijing Key Laboratory of Radiation Advanced Materials, Beijing Research Center for Radiation Application Co.,Ltd., Beijing 100015, China. E-mail: daipei008@126.com*

combine with Cu^{2+} in Cu-BTC to form a glyphosate–Cu^{2+} complex, thereby inhibiting the current response. However, due to the poor conductivity of Cu-BTC, its direct application in electrochemical sensing still has a lot of limitations. Therefore, combining Cu-BTC with other conductive materials to amplify the sensing signal and improve the electrochemical sensing performance is a promising method.[35,36] As a new type of two-dimensional nanomaterial, MXenes not only has the characteristics of large specific surface area, outstanding hydrophilicity and abundant surface functional groups, but more importantly, it has ultra-high conductivity.[37–41] Its combination with Cu-BTC compounding can give full play to the synergistic effect of the two, which is of great significance in the electrochemical sensing of glyphosate.

In this article, two-dimensional material $Ti_3C_2T_x$ was first prepared by chemical etching, then Cu-BTC was grown by *in situ* growth method using $Ti_3C_2T_x$ nanosheets as a template, and finally, the prepared $Ti_3C_2T_x$/Cu-BTC nanocomposite was passed through the adsorption method to be modified on a glassy carbon electrode (GCE), constructing an electrochemical sensor for glyphosate detection to achieve high-efficiency sensing of glyphosate.

2. Experimental section

2.1. Materials

Ti_3AlC_2 powder (400 mesh) was obtained from 11 Technology Co., Ltd (JiLin, China). $Co(NO_3)_2 \cdot 6H_2O$, 2-methylimidazole, glyphosate, NaOH, KCl and NaCl were purchased from Beijing Chemical Works (China). Lithium fluoride (LiF, 98.5%), hydrochloric acid (HCl, 37%) were bought from Sigma Aldrich. All chemicals were of analytical grade and used as received without further purification.

2.2. Preparation of $Ti_3C_2T_x$

Add 1 g of lithium fluoride to a polypropylene plastic bottle containing 20 ml of 9 M hydrochloric acid, and continue stirring for 0.5 h to ensure that the lithium fluoride is completely dissolved. Slowly add 1 g Ti_3AlC_2 to the hydrochloric acid solution in which lithium fluoride is dissolved, and then stir the reaction at 35 °C for 48 h, and wash the etching product with deionized water until the supernatant pH $\geq$ 6 to obtain multilayer $Ti_3C_2T_x$. Under the conditions of ice-water bath and argon protection, the multilayer $Ti_3C_2T_x$ solution was sonicated for 1 h, and then centrifuged at a speed of 3500 rpm to obtain a monolayer/small-layer $Ti_3C_2T_x$ dispersion. The obtained single-layer/small-layer $Ti_3C_2T_x$ dispersion was freeze-dried for 48 h to obtain $Ti_3C_2T_x$ nanosheets.

2.3. Preparation of Cu-BTC

The synthesis of pure Cu-BTC followed that described in the literature.[31] 1,3,5-Trimesic acid (0.875 g) and copper nitrate trihydrate (1.82 g) were respectively dissolved in 50 ml methanol solvent to prepare mixed solutions A and B, and stir for 0.5 h respectively. Then add mixed solution B to mixed solution A, stir vigorously for 5 min, and then stand at room temperature for 24 h. Finally, the product obtained after standing was centrifuged and washed with methanol, and the Cu-BTC was obtained by freeze-drying for 24 h.

2.4. Preparation of $Ti_3C_2T_x$/Cu-BTC composite

Solutions A and B were prepared in "2.3. Preparation of Cu-BTC". Measure 10 ml $Ti_3C_2T_x$ aqueous solution (5 mg ml^{-1}), and slowly add it to the mixed solution B, and continue to stir for 0.5 h. After the stirring, add mixed solution A, stir vigorously for 5 min, and then stand at room temperature for 24 h. Finally, the product obtained after standing was centrifuged and washed with methanol, and the $Ti_3C_2T_x$/Cu-BTC composite was obtained by freeze-drying for 24 h.

2.5. Preparation of $Ti_3C_2T_x$/Cu-BTC/GCE

Grind and polish the glassy carbon electrode (GCE) to a mirror-like surface with 0.05 μm and 0.3 μm alumina powder, respectively. Weigh 10 mg of $Ti_3C_2T_x$/Cu-BTC composite and ultrasonically disperse it in 5 ml of ethanol, then use a pipette to pipette 10 μL of the dispersion onto the surface of GCE, and dry it in a vacuum oven for 10 min (room temperature) to get $Ti_3C_2T_x$/Cu-BTC/GCE.

2.6. Instrumentation and measurements

The morphologies of the samples were observed by scanning electron microscopy (SEM, SU8020). X-ray powder diffraction (XRD) spectra analyses the crystal structure of samples were carried out by the Bruker D8 with a Cu Kα radiation at a scan speed of 5° min^{-1} and a step size of 0.02°. X-ray photoelectron spectroscopy (XPS) analyses of the $Ti_3C_2T_x$/Cu-BTC nanocomposite were carried out by the Thermo ESCLAB 250 Xi (ThermoFisher Scientific, USA). The automatic specific surface and porosity analyzer model (ASAP 2020) was used to characterize the specific surface area of samples. All electrochemical properties were recorded by the IviumStat Electrochemical Workstation with a three electrodes system. In this system, the glassy carbon electrode (GCE) was used as the working electrode, and Ag/AgCl and platinum flat were employed as the reference and counter electrode, respectively.

3. Results and discussion

3.1. Formation of $Ti_3C_2T_x$/Cu-BTC nanocomposite

The preparation process of $Ti_3C_2T_x$/Cu-BTC composite is shown in Fig. 1 clearly. $Ti_3C_2T_x$–MXene nanosheets are obtained by etching and stripping the MAX phase Ti_3AlC_2 in the beginning. Then using $Ti_3C_2T_x$ nanosheets as a template to grow Cu-BTC *in situ* to obtain $Ti_3C_2T_x$/Cu–BTC complex. During the *in situ* growth of Cu-BTC, Cu^{2+} is adsorbed on the surface by the electrostatic effect. In the end, the O atoms of trimesic acid and Cu^{2+} rapidly nucleate through coordination reaction on the surface of $Ti_3C_2T_x$ nanosheets, and grow into Cu-BTC to obtain $Ti_3C_2T_x$/Cu-BTC composites.

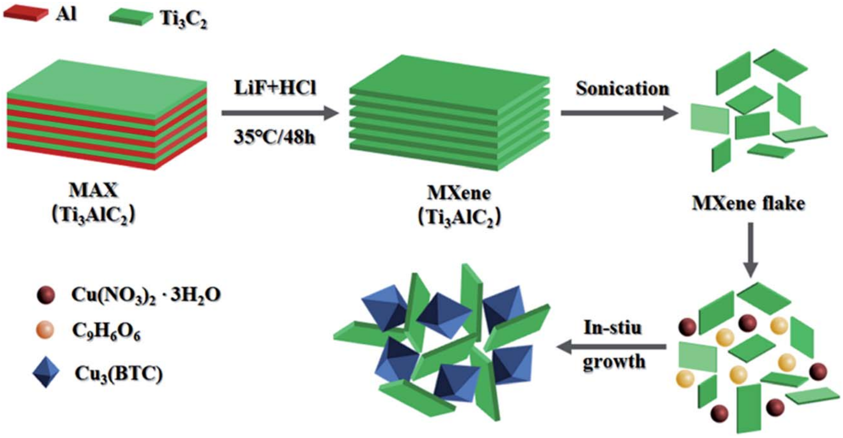

Fig. 1 The preparation of $Ti_3C_2T_x$/Cu-BTC composite.

3.2. Morphology of $Ti_3C_2T_x$/Cu-BTC nanocomposite

Fig. 2(a) is SEM image of the precursor MAX phase Ti_3AlC_2. It exhibited that Ti_3AlC_2 has a tightly stacked three-dimensional layered structure. When the Al layer in Ti_3AlC_2 is etched and eliminated, a multilayer $Ti_3C_2T_x$ with an accordion-like structure formed by weak van der Waals forces or hydrogen bonds is obtained, as shown in Fig. 2(b). Fig. 2(c) is the TEM image of the single-layer/small-layer $Ti_3C_2T_x$ nanosheets obtained after ultrasonic peeling of multilayer $Ti_3C_2T_x$. It can be seen that the multilayer $Ti_3C_2T_x$ is ultrasonically peeled to obtain a thin to transparent single layer or stack of single layers. Fig. 2(d) is the SEM image of the Cu-BTC sample. It can be seen that the Cu-BTC cubic crystal is a typical octahedral geometry, and its size is about 2 μm. Fig. 2(e) and (f) are the SEM images of $T_3C_2T_x$/Cu-BTC composites under different magnifications. It can be seen that $Ti_3C_2T_x$ does not affect the growth of Cu-BTC crystals, but it is different from $Ti_3C_2T_x$/ZIF-8 and $Ti_3C_2T_x$/ZIF-67. The difference is because the size of Cu-BTC is equal to or larger than $Ti_3C_2T_x$ nanosheets, the $Ti_3C_2T_x$/Cu-BTC nanocomposite is finally presented in the form of $Ti_3C_2T_x$ nanosheets interspersed between Cu-BTC.

EDS element mapping analysis on the $Ti_3C_2T_x$/Cu-BTC nanocomposite was carried out to explore its element composition and distribution. Fig. 3(a) is the SEM image of $Ti_3C_2T_x$/Cu-BTC composite material. To perform EDS element mapping analysis in this area, and the EDS element mapping spectrum containing the elements Ti, Cu, C and O was obtained. Fig. 3(c–f) are EDS element maps of independent elements (Ti, Cu, C and O). Ti element belongs to $Ti_3C_2T_x$, Cu element is the characteristic element of Cu-BTC, and C and O elements are at the same time existing in $Ti_3C_2T_x$ and Cu-BTC, which further indicates the successful preparation of $Ti_3C_2T_x$/Cu-BTC composites.

3.3. Crystal structure of $Ti_3C_2T_x$/Cu-BTC nanocomposite

Fig. 4 shows the X-ray diffraction spectrum of Ti_3AlC_2, $Ti_3C_2T_x$, Cu-BTC and $Ti_3C_2T_x$/Cu-BTC nanocomposites. The X-ray diffraction spectrum of MAX phase Ti_3AlC_2 shows all the characteristic peaks, among which the diffraction peaks at 9.58°, 19.2° and 39.04° correspond to the (002), (004) and (104) characteristic peaks of crystal Ti_3AlC_2, respectively. The X-ray diffraction pattern of $Ti_3C_2T_x$ showed that the characteristic

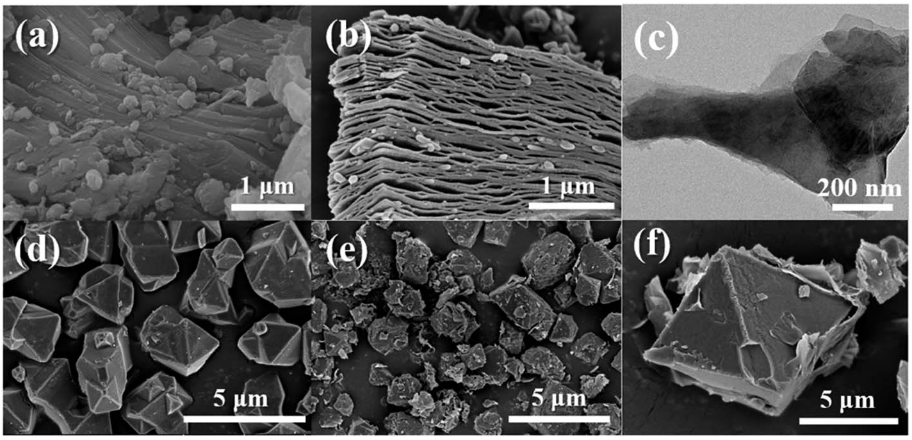

Fig. 2 SEM images of (a) Ti_3AlC_2, (b) multilayer $Ti_3C_2T_x$, (d) Cu-BTC, (e) and (f) $Ti_3C_2T_x$/Cu-BTC; (c) TEM images of monolayer/small-layer $Ti_3C_2T_x$ nanosheets.

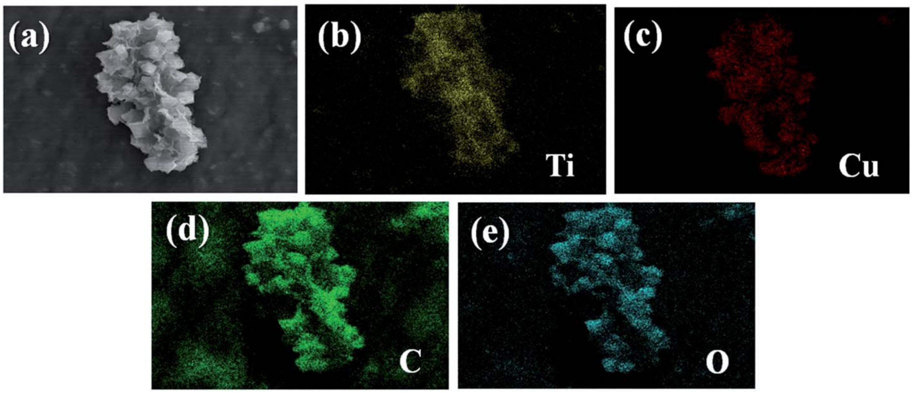

Fig. 3 SEM image (a) and EDS element map (b–e) of $Ti_3C_2T_x$/Cu-BTC nanocomposite.

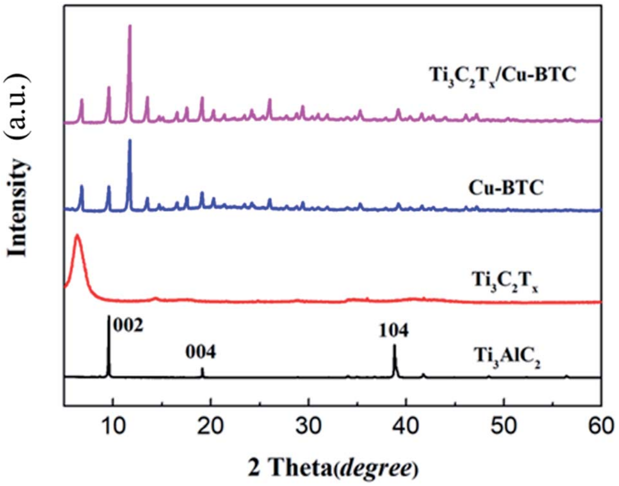

Fig. 4 X-ray diffraction patterns of Ti_3AlC_2, $Ti_3C_2T_x$, Cu-BTC and $Ti_3C_2T_x$/Cu-BTC.

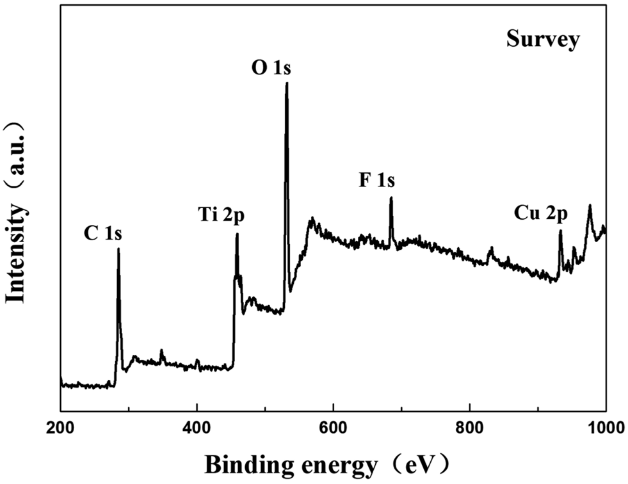

Fig. 5 XPS full spectrum of $Ti_3C_2T_x$/Cu-BTC composite.

peaks (004 and 104) of Ti_3AlC_2 disappeared, and the diffraction peak (002) shifted to a smaller angle, proving that Ti_3AlC_2 was successfully etched into $Ti_3C_2T_x$. The characteristic peaks of X-ray diffraction of Cu-BTC and the characteristic peaks of Cu-BTC reported can match well, which proves the successful preparation of Cu-BTC. The X-ray diffraction pattern of $Ti_3C_2T_x$/Cu-BTC can well identify the diffraction characteristic peaks of Cu-BTC and $Ti_3C_2T_x$, which indicates that the presence of $Ti_3C_2T_x$ will not affect the growth of Cu-BTC crystals, which further indicates successful preparation of $Ti_3C_2T_x$/Cu-BTC composite material.

The surface properties of the $Ti_3C_2T_x$/Cu-BTC composite were further studied by XPS. Fig. 5 shows the XPS full spectrum of the $Ti_3C_2T_x$/Cu-BTC composite. It can be seen from the figure that the six peaks of $Ti_3C_2T_x$/Cu-BTC at 298 eV, 475 eV, 545 eV, 685 eV and 965 eV correspond to the elements C 1s, Ti 2p, O 1s, F 1s and Cu 2p, respectively. Cu 2p is a characteristic element of Cu-BTC and Ti 2p was derived from $Ti_3C_2T_x$, which was similar with the XPS spectra of $Ti_3C_2T_x$ (ref. 41–43) and Cu-BTC.[30,44,45] The characterization result further indicated the successful preparation of $Ti_3C_2T_x$/Cu-BTC composites.

3.4. Surface area and porosity of $Ti_3C_2T_x$/Cu-BTC nanocomposite

In order to further analyze the pore structure of Cu-BTC and $Ti_3C_2T_x$/Cu-BTC composites, the surface area and pore size distribution of Cu-BTC and $Ti_3C_2T_x$/Cu-BTC were tested. The results are shown in Table 1 and Fig. 6. Fig. 6(a) and (c) are the N_2 adsorption–desorption isotherms of Cu-BTC and $Ti_3C_2T_x$/Cu-BTC, respectively. It can be seen that both Cu-BTC and $Ti_3C_2T_x$/Cu-BTC are typical I-type adsorption isotherms. The curve shows that Cu-BTC and $Ti_3C_2T_x$/Cu-BTC are both microporous structures. At the same time, Fig. 6(b) and (d) are the pore size distribution curves of Cu-BTC and $Ti_3C_2T_x$/Cu-BTC, respectively. It can be seen that the pore size distribution is mainly concentrated around 1.5 nm, which is consistent with the corresponding adsorption–desorption isotherms.

It can be seen from Table 1 that the average pore diameter of Cu-BTC and $Ti_3C_2T_x$/Cu-BTC composite materials are both about 1.5 nm, which shows that the addition of $Ti_3C_2T_x$ nanosheets does not affect the formation of Cu-BTC crystals. In addition, the specific surface areas of Cu-BTC and $Ti_3C_2T_x$/Cu-BTC are 1511 m^2 g^{-1} and 874 m^2 g^{-1}, respectively. The

Table 1 Surface area and average pore diameter of Cu-BTC and $Ti_3C_2T_x$/Cu-BTC composite

Sample name	Surface area (m^2 g^{-1})	Average pore size (nm)
Cu-BTC	1511	1.525
$Ti_3C_2T_x$/Cu-BTC	874	1.593

specific surface area of $Ti_3C_2T_x$/Cu-BTC is smaller than that of Cu-BTC because $Ti_3C_2T_x$ nanosheets with a dense film structure do not contribute much to the specific surface area during the specific surface area test, and the decrease in the proportion of Cu-BTC in the unit mass results in that specific surface area of $Ti_3C_2T_x$/Cu-BTC is lower than pure Cu-BTC.

3.5. Electrochemical impedance analysis of $Ti_3C_2T_x$/Cu-BTC/GCE

As shown in Fig. 7, the conductivity of GCE modified with different materials was analyzed by electrochemical impedance spectroscopy (EIS). It can be seen from the figure that bare GCE shows a large semicircular area at high frequency, and Cu-BTC/GCE shows a larger semicircular area, and its semicircular diameter further increases, which proves the inherent insulation properties of Cu-BTC. Compared with GCE and Cu-BTC/GCE, the EIS spectrum of $Ti_3C_2T_x$/GCE has no obvious semicircular area, even close to linearity, which further shows that $Ti_3C_2T_x$ has ultra-high electrical conductivity. For $Ti_3C_2T_x$/Cu-BTC/GCE, the semicircle diameter is between that of $Ti_3C_2T_x$/GCE and GCE, which shows that $Ti_3C_2T_x$ can effectively improve the low conductivity characteristics of Cu-BTC. The combination of $Ti_3C_2T_x$ and Cu-BTC exhibited excellent synergy. On one hand, Cu-BTC as the matrix could fix and disperse the $Ti_3C_2T_x$ to prohibit $Ti_3C_2T_x$ aggregation. On the other hand, $Ti_3C_2T_x$ loading on the Cu-BTC is helpful to enhance the conductivity and electrocatalytic activity. So a fast electronic channel in $Ti_3C_2T_x$/Cu-BTC is formed between the electrode and the electrolyte, which is expected to become a good platform for sensing applications.

3.6. Electrochemical behaviors of $Ti_3C_2T_x$/Cu-BTC/GCE

The electrochemical behaviors of $Ti_3C_2T_x$/Cu-BTC nanocomposite between different modified electrodes and glyphosate in 0.1 M phosphate-buffered saline (PBS) were measured by cyclic voltammetry to analyze the applicability for electrochemical sensing of glyphosate. Fig. 8 shows the cyclic voltammetry curves of GCE, Cu-BTC/GCE and $Ti_3C_2T_x$/Cu-BTC/GCE with and without glyphosate added to 0.1 M PBS electrolyte. It can be seen from the figure that the graph of bare GCE is a smooth curve without obvious redox peaks. Compared with

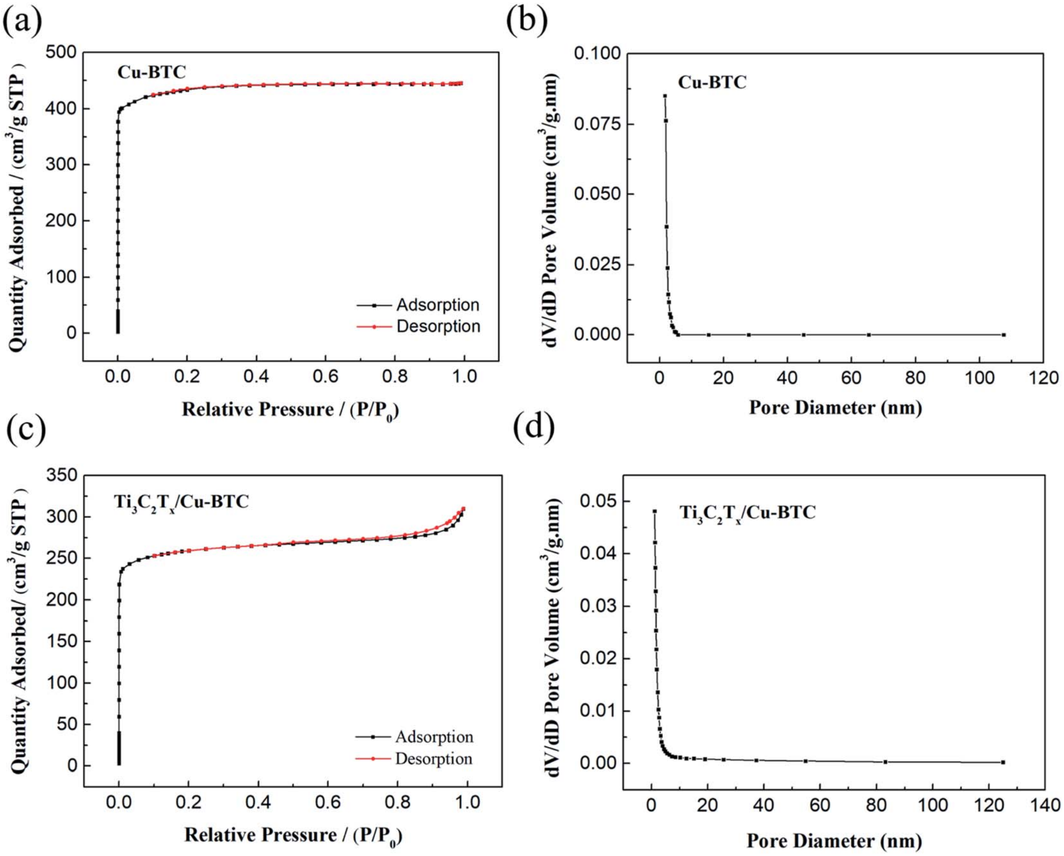

Fig. 6 (a) Cu-BTC and (c) $Ti_3C_2T_x$/Cu-BTC N_2 adsorption–desorption isotherms; (b) Cu-BTC and (d) $Ti_3C_2T_x$/Cu-BTC pore size distribution curves.

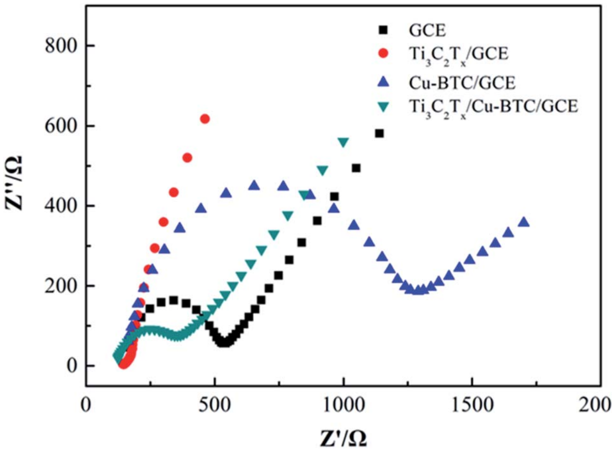

Fig. 7 EIS Nyquist plots of GCE, $Ti_3C_2T_x$/GCE, Cu-BTC/GCE and $Ti_3C_2T_x$/Cu-BTC/GCE.

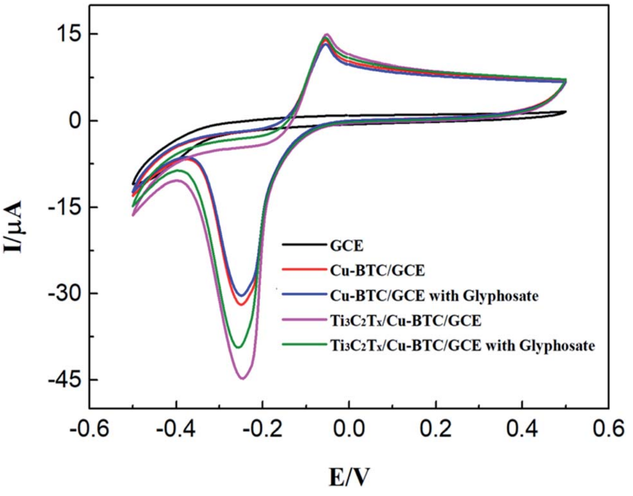

Fig. 8 (a) The cyclic voltammetry graph of bare/GCE, Cu-BTC/GCE, $Ti_3C_2T_x$/Cu-BTC/GCE in 0.1 M phosphate-buffered saline (PBS) with and without glyphosate.

bare GCE, the graph of Cu-BTC/GCE has a pair of obvious redox peaks, which are formed by the mutual conversion of Cu(II) and Cu(I). In addition, compared with Cu-BTC/GCE, the graph of $Ti_3C_2T_x$/Cu-BTC/GCE also has similar redox peaks, and its response peak current is much larger than Cu-BTC/GCE, which can be attributed to the high conductivity of $Ti_3C_2T_x$ nanosheets greatly improving the inherent weak conductivity of Cu-BTC, and therefore $Ti_3C_2T_x$/Cu-BTC/GCE has a higher electron transfer rate.

When glyphosate is added to the PBS electrolyte, the oxidation peak currents of Cu-BTC/GCE and $Ti_3C_2T_x$/Cu-BTC/GCE are reduced. This is due to the coordination of Cu-BTC and glyphosate, which inhibits the mutual conversion of Cu(II) and Cu(I) in Cu-BTC, leading to a decrease in response current. It is worth noting that, compared with Cu-BTC/GCE, the peak response current of $Ti_3C_2T_x$/Cu-BTC/GCE is significantly reduced. Because the glyphosate electrochemical sensor realizes the electrochemical detection of glyphosate through the difference in response current shown by the blank sample and the sample with glyphosate added. Therefore, compared with Cu-BTC, $Ti_3C_2T_x$/Cu-BTC/GCE has a larger response peak current and a more obvious response current difference, which has advantages in the electrochemical sensing of glyphosate.

3.7. Quantitative sensing of glyphosate by $Ti_3C_2T_x$/Cu-BTC/GCE

Differential pulse voltammetry (DPV) is of great significance in the sensory analysis of ultra-low concentration analytes. $Ti_3C_2T_x$/Cu-BTC/GCE showed excellent sensing performance in the cyclic voltammetry test of glyphosate. The analyte glyphosate was further analyzed quantitatively by DPV method, and the results are shown in Fig. 9. When the concentration of glyphosate is 0, it shows a higher response peak current. As the concentration of glyphosate increases from 0 to 1×10^{-13} M, the response peak current gradually decreases. This is because as the concentration of glyphosate increases, the more glyphosate–Cu^{2+} complex will be formed. Fig. 9(b) shows the relationship between the current peak value change (ΔI) and the glyphosate concentration. It can be seen that the current peak

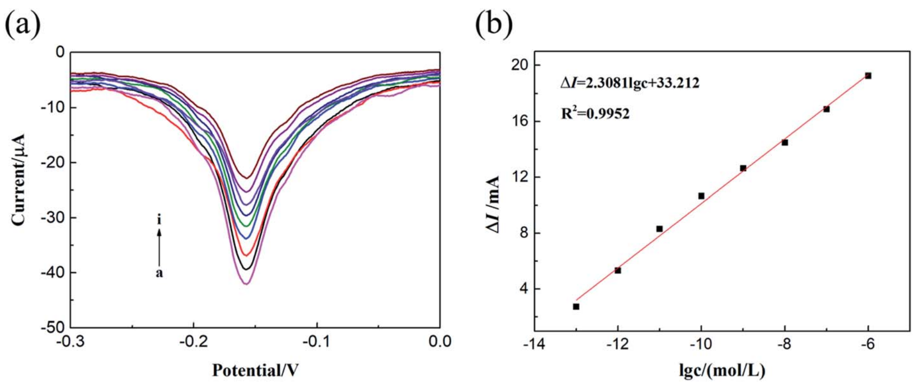

Fig. 9 (a) DPV curve of $Ti_3C_2T_x$/Cu-BTC/GCE with different concentrations of glyphosate, (a–i) (0; 1.0×10^{-13}; 1.0×10^{-12}; 1.0×10^{-11}; 1.0×10^{-10}; 1.0×10^{-9}; 1.0×10^{-8}; 1.0×10^{-7}; 1.0×10^{-6}) (b) the logarithmic relationship between the response current peak change value (ΔI) and the glyphosate concentration.

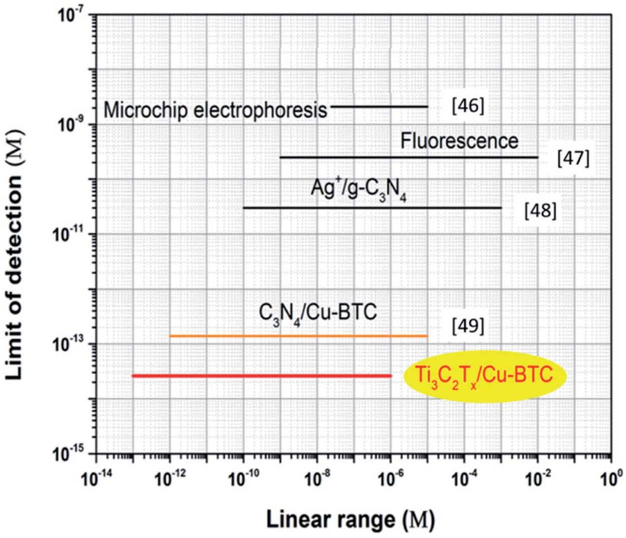

Fig. 10 Comparison of detection range and detection limit of $Ti_3C_2T_x$/Cu-BTC and other glyphosate sensors.[46–49]

change value (ΔI) is linearly related to the glyphosate concentration, and the linear range is 1.0×10^{-1} to 1.0×10^{-6} M, the linear regression equation is $\Delta I = 2.3081 \lg c + 33.212$. In addition, the limit of detection based on $Ti_3C_2T_x$/Cu-BTC/GCE calculated by the glyphosate sensor is 2.6×10^{-14} M. This indicates that the glyphosate electrochemical sensor based on $Ti_3C_2T_x$/Cu-BTC composite material has a wide linear response range and a low detection limit. The excellent detection performance of the sensor is attributed to the excellent conductivity of $Ti_3C_2T_x$ and the unique interaction between Cu-BTC and glyphosate.

Fig. 10 shows the comparison of the detection range and detection limit of $Ti_3C_2T_x$/Cu-BTC and other glyphosate testing equipment.[46–49] It can be seen that $Ti_3C_2T_x$/Cu-BTC has the lowest LOD (2.6×10^{-14} M) while ensuring a wide detection range (1.0×10^{-13} to 1.0×10^{-6} M). It is worth noting that the limit of detection based on $Ti_3C_2T_x$/Cu-BTC is even lower than that of the C_3N_4/Cu-BTC sensor (1.3×10^{-13} M)[49] with the same modification of Cu-BTC. The good detection performance of $Ti_3C_2T_x$/Cu-BTC is contributed by the high conductivity of $Ti_3C_2T_x$ and the strong interaction of Cu-BTC and glyphosate. All the above shows that $Ti_3C_2T_x$/Cu-BTC has obvious advantages as a sensor for detecting glyphosate. It means that $Ti_3C_2T_x$/Cu-BTC is an effective electrode material and has great potential in glyphosate detection.

3.8. Sensing mechanism of glyphosate by $Ti_3C_2T_x$/Cu-BTC/GCE

As shown in Fig. 11, $Ti_3C_2T_x$/Cu-BTC/GCE showed excellent electrochemical sensing performance for glyphosate. The $Ti_3C_2T_x$/Cu-BTC nanocomposite material was modified on the surface of the glass carbon electrode (GCE) by the drop-casting method to obtain $Ti_3C_2T_x$/Cu-BTC/GCE. In the electrochemical sensing process of glyphosate, the synergistic effect of the $Ti_3C_2T_x$/Cu-BTC nanocomposite material greatly promotes the electrochemical sensing effect of glyphosate. In this process, the oxidation–reduction reaction of Cu-BTC (the mutual conversion of Cu(ɪɪ) and Cu(ɪ)) generates a response current. When glyphosate is added or the concentration of glyphosate increases, the phosphate groups, secondary amino groups and carboxyl groups in glyphosate have a strong affinity for Cu^{2+} in Cu-BTC, and glyphosate is easily adsorbed on the metal structure center of Cu-BTC to form a glyphosate–Cu^{2+} complex, which hinders the transfer of electrons and reduces the response current. The response current reduction value is proportional to the

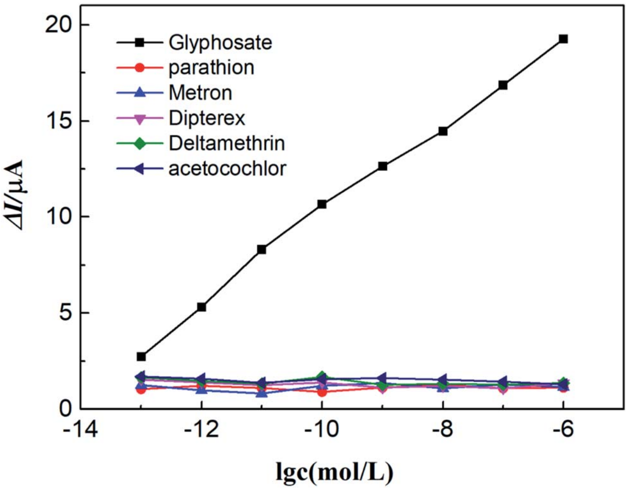

Fig. 12 The relationship between the ΔI of $Ti_3C_2T_x$/Cu-BTC/GCE for different detection substances and the logarithm of concentration.

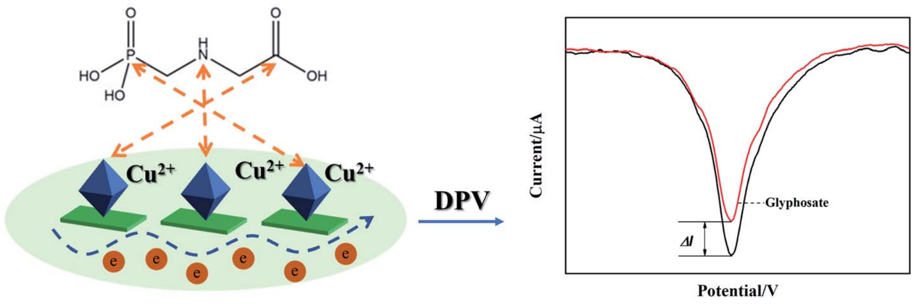

Fig. 11 $Ti_3C_2T_x$/Cu-BTC/GCE detection mechanism of glyphosate.

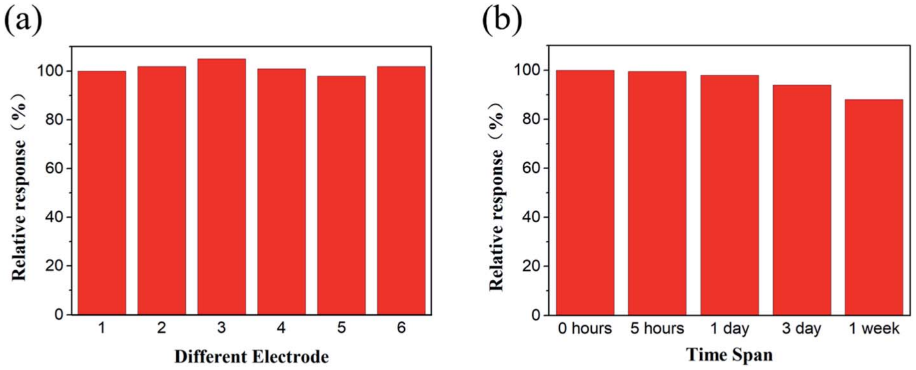

Fig. 13 $Ti_3C_2T_x$/Cu-BTC/GCE reproducibility (a) and stability (b).

glyphosate concentration, and the glyphosate concentration is evaluated based on the change in the response current before and after the reaction.

It is worth mentioning that due to the inherent insulation of Cu-BTC, the electrochemical detection of glyphosate using Cu-BTC alone has problems such as low response current and small current change. Introduction of 2D nanosheet into basic material could supply good sensitivity since 2D nanomaterials are used as the channel material to fabricate sensor.[50] Therefore by combining $Ti_3C_2T_x$ with high conductivity and Cu-BTC, the conductivity of Cu-BTC can be greatly improved, the response current and current change value can be increased, and the sensing signal can be significantly amplified.

3.9. Anti-interference, reproducibility and stability of $Ti_3C_2T_x$/Cu-BTC/GCE

Anti-interference is an important performance of electrochemical sensors in practical applications. The differential pulse voltammetry (DPV) was employed to investigate the interference substances that may exist in practical applications of glyphosate electrochemical sensors based on $Ti_3C_2T_x$/Cu-BTC. Evaluation of anti-jamming performance. To research the selectivity of $Ti_3C_2T_x$/Cu-BTC to glyphosate, five common pesticides including parathion, metron, Dipterex, deltamethrin and acetochlor were selected as interference substances. In the anti-interference performance test, except that glyphosate was replaced with the same concentration of interfering substances, the other test conditions remained relatively consistent. Fig. 12 shows the relationship of current peak change value (ΔI) and corresponding sensor concentration (logarithm) of $Ti_3C_2T_x$/Cu-BTC to glyphosate, parathion, metron, Dipterex, deltamethrin and acetochlor. It can be seen from Fig. 12 that as the concentration of the detection substance increases, only the ΔI corresponding to glyphosate increases and shows a relatively linear relationship, while the ΔI of other detection substances is very small and almost remains unchanged. Therefore, the prepared $Ti_3C_2T_x$/Cu-BTC/GCE sensor has excellent anti-interference ability in the electrochemical detection of glyphosate.

The reproducibility of the sensor was explored by continuously testing 6 $Ti_3C_2T_x$/Cu-BTC/GCE of the same batch under the same conditions. As shown in Fig. 13(a), the relative standard deviation of the obtained response current is 2.3%, which indicates that the sensor has good reproducibility. In order to further study the stability of the prepared sensor, the prepared $Ti_3C_2T_x$/Cu-BTC/GCE was stored in the same storage environment for 5 hours, 1 day, 3 days and 1 week, according to the activity change of the sensor after different storage time to evaluate the stability of the sensor. As shown in Fig. 13(b), the sensor still retains 88.6% of its activity after 1 week of storage, indicating that the sensor has excellent stability.

4. Conclusions

In conclusion, this paper reported the preparation of an electrochemical sensor based on $Ti_3C_2T_x$/Cu-BTC for the electrochemical sensing of glyphosate using a facile method for the first time. The electrochemical sensor based on $Ti_3C_2T_x$/Cu-BTC combines the advantages of high electric conductivity and unique electrocatalytic activity, thus having high sensing performance for glyphosate, including a low limit of detection (2.6×10^{-14} M) and wide linear response range (1.0×10^{-13} to 1.0×10^{-6} M). In addition, experimental results show that it also has good stability and anti-interference. This work demonstrates that the combination of the electrocatalytic activity of MOF and 2D $Ti_3C_2T_x$ with ultra-high conductivity is a promising method for the development of high-performance electrochemical sensors.

Conflicts of interest

There are no conflicts to declare.

Acknowledgements

This study was funded by National Natural Science Foundation of China (11805016) and Beijing Nova Program (Z201100006820113).

References

1 A. H. C. Van Bruggen, M. M. He, K. Shin, V. Mai, K. C. Jeong, M. R. Finckh and J. G. Morris, *Sci. Total Environ.*, 2018, **616–617**, 255–268.

2 D. la Cecilia and F. Maggi, *Environ. Pollut.*, 2018, **233**, 201–207.

3 N. Corrales, M. Meerhoff and D. Antoniades, *Environ. Pollut.*, 2021, **284**, 117354.

4 K. Gandhi, S. Khan, M. Patrikar, A. Markad, N. Kumar, A. Choudhari, P. Sagar and S. Indurkar, *Environ. Challenges*, 2021, **4**, 100149.

5 V. N. Dhamu and S. Prasad, *Biosens. Bioelectron.*, 2020, **170**, 112609.

6 A. Connolly, M. A. Coggins and H. M. Koch, *Toxics*, 2020, **8**, 1–18.

7 C. Zhang, X. Liang, Y. Lu, H. Li and X. Xu, *Sensors*, 2020, **20**, 4146.

8 Y. Yao, X. Han, X. Yang, J. Zhao and C. Chai, *Chin. J. Chem.*, 2021, **39**, 330–336.

9 L. Wang, Q. Teng, X. Sun, Y. Chen, Y. Wang, H. Wang and Y. Zhang, *J. Colloid Interface Sci.*, 2018, **512**, 127–133.

10 W. Meng, Y. Wen, L. Dai, Z. He and L. Wang, *Sens. Actuators, B*, 2018, **260**, 852–860.

11 M. Zarejousheghani, A. Jaafar, H. Wollmerstaedt, P. Rahimi, H. Borsdorf, S. Zimmermann and Y. Joseph, *Sensors*, 2021, **21**, 1–18.

12 J. C. Ulrich and P. L. Ferguson, *Anal. Bioanal. Chem.*, 2021, **413**, 3763–3774.

13 A. L. Valle, F. C. C. Mello, R. P. Alves-Balvedi, L. P. Rodrigues and L. R. Goulart, *Environ. Chem. Lett.*, 2019, **17**, 291–317.

14 B. B. Prasad, D. Jauhari and M. P. Tiwari, *Biosens. Bioelectron.*, 2014, **59**, 81–88.

15 A. Khenifi, Z. Derriche, C. Forano, V. Prevot, C. Mousty, E. Scavetta, B. Ballarin, L. Guadagnini and D. Tonelli, *Anal. Chim. Acta*, 2009, **654**, 97–102.

16 T. Rijnaarts, R. Mejia-Ariza, R. J. M. Egberink, W. van Roosmalen and J. Huskens, *Chem.–Eur. J.*, 2015, **21**, 10296–10301.

17 Q. L. Zhu and Q. Xu, *Chem. Soc. Rev.*, 2014, **43**, 5468–5512.

18 R. R. Salunkhe, Y. V. Kaneti, J. Kim, J. H. Kim and Y. Yamauchi, *Acc. Chem. Res.*, 2016, **49**, 2796–2806.

19 Y. Zhao, M. Seredych, J. Jagiello, Q. Zhong and T. J. Bandosz, *Chem. Eng. J.*, 2014, **239**, 399–407.

20 X. Zhang, X. Wang, W. Fan and D. Sun, *Chin. J. Chem.*, 2020, **38**, 509–524.

21 Y. Z. Chen, R. Zhang, L. Jiao and H. L. Jiang, *Coord. Chem. Rev.*, 2018, **362**, 1–23.

22 D. Cheng, X. Xiao, X. Li, C. Wang, Y. Liang, Z. Yu, C. Jin, N. Zhou, M. Chen, Y. Dong, Y. Lin, Z. Xie and C. Zhang, *J. Electrochem. Soc.*, 2018, **165**, B885–B892.

23 S. Rani, B. Sharma, R. Malhotra, S. Kumar, R. S. Varma and N. Dilbaghi, *Environ. Res.*, 2020, **191**, 110005.

24 G. Yu, J. Xia, F. Zhang and Z. J. Wang, *Electroanal. Chem.*, 2017, **801**, 496–502.

25 Y. Yuan, J. Xia, F. Zhang, Z. Wang and Q. J. Liu, *Electroanal. Chem.*, 2018, **824**, 147–152.

26 M. Sohail, M. Altaf, N. Baig, R. Jamil, M. Sher and A. Fazal, *New J. Chem.*, 2018, **42**, 12486–12491.

27 M. Annalakshmi, P. Balasubramanian, S. M. Chen and T. W. Chen, *Sens. Actuators, B*, 2019, **296**, 126620.

28 Y. Song, C. Gong, D. Su, Y. Shen, Y. Song and L. Wang, *Anal. Methods*, 2016, **8**, 2290–2296.

29 S. Wu, Z. Song, M. Zhu, Y. Zhang, W. Yao, M. Kosinova, V. P. Fedin, J. Chen and E. Gao, *Appl. Organomet. Chem.*, 2021, **35**, 1–11.

30 C. Li and K. Wu, *Anal. Chim. Acta*, 2021, **1162**, 338473.

31 S. S. Y. Chui, S. M. F. Lo, J. P. Charmant, A. G. Orpen and I. D. Williams, *Science*, 1999, **283**, 1148–1150.

32 X. Zhang, J. Luo, P. Tang, J. R. Morante, J. Arbiol, C. Xu, Q. Li and J. Fransaer, *Sens. Actuators, B*, 2018, **254**, 272–281.

33 L. Ji, Q. Cheng, K. Wu and X. Yang, *Sens. Actuators, B*, 2016, **231**, 12–17.

34 Y. Cao, L. Wang, C. Shen, C. Wang, X. Hu and G. Wang, *Sens. Actuators, B*, 2019, **283**, 487–494.

35 Y. Wang, C. Hou, Y. Zhang, F. He, M. Liu and X. Li, *J. Mater. Chem. B*, 2016, **4**, 3695–3702.

36 E. Zhou, Y. Zhang, Y. Li and X. He, *Electroanalysis*, 2014, **26**, 2526–2533.

37 H. Liu, C. Duan, C. Yang, W. Shen, F. Wang and Z. Zhu, *Sens. Actuators, B*, 2015, **218**, 60–66.

38 Z. Xue, L. Jia, R. R. Zhu, L. Du and Q. H. J. Zhao, *Electroanal. Chem.*, 2020, **858**, 113783.

39 R. B. Rakhi, P. Nayuk, C. Xia and H. N. Alshareef, *Sci. Rep.*, 2016, **6**, 1–10.

40 R. A. Soomro, S. Jawaid, Q. Zhu, Z. Abbas and B. Xu, *Chin. Chem. Lett.*, 2020, **31**, 922–930.

41 M. Naguib, M. Kurtoglu, V. Presser, J. Lu, J. Niu, M. Heon, L. Hultman, Y. Gogotsi and M. W. Barsoum, *Adv. Mater.*, 2011, **23**, 4248–4253.

42 X. Zhou, Y. Guo, D. Wang and Q. Xu, Nano friction and adhesion properties on Ti_3C_2 and Nb_2C MXene studied by AFM, *Tribol. Int.*, 2021, **53**, 106646.

43 Y. J. Mai, Y. G. Li, S. L. Li, L. Y. Zhang, C. S. Liu and X. H. Jie, *J. Alloys Compd.*, 2019, **770**, 1–5.

44 H. Shu, Y. Liu and Y. Jia, Synthesis of Cu-BTC by room temperature hydrothermal and its low temperature SCR denitration, *J. Mol. Struct.*, 2022, **1251**, 132046.

45 N. Torres, J. Galicia, Y. Plasencia, A. Cano, F. Echevarría, L. F. Desdin-Garcia and E. Reguera, Implications of structural differences between Cu-BTC and Fe-BTC on their hydrogen storage capacity, *Colloids Surf., A*, 2018, **549**, 138–146.

46 X. Wei, X. Gao, L. Zhao, X. Peng, L. Zhou, J. Wang and Q. Pu, *J. Chromatogr. A*, 2013, **1281**, 148–154.

47 Y. Zhang, Y. Zhang, Q. Qu, G. Wang and C. Wang, *Anal. Methods*, 2013, **5**, 6465–6472.

48 Y. Li, S. Zhang, Q. Zhang, G. Xu, H. Dai and Y. Lin, *Sens. Actuators, B*, 2016, **224**, 798–804.

49 Y. Cao, L. Wang, C. Wang, X. Hu, Y. Liu and G. Wang, *Electrochim. Acta*, 2019, **317**, 341–347.

50 J. Zha, Z. Yuan, Z. Zhou, Y. Li, J. Zhao, Z. Zeng, L. Zhen, H. Tai, C. Tan and H. Zhang, *Small Struct.*, 2021, 2100067.